Distributed Acoustic Sensing for aftershock monitoring: the case of the 2019 M_w 4.9 Le Teil earthquake

van den Ende M. P. A., Ampuero J.-P., Courboulex F., Delouis B., Godano M., Larroque C., Sladen A.

This manuscript has been submitted for publication in *Seismica*. Subsequent versions of this manuscript may have different content. If accepted, the final version of this manuscript will be available via the *Peer-reviewed Publication DOI* link printed on this webpage.

All the data and scripts needed to reproduce the results are publicly available from:

> van den Ende M. P. A., Ampuero J.-P., Courboulex F., Delouis B., Godano M., Larroque C., Sladen A. (2024): *Data and scripts for: Distributed Acoustic Sensing for aftershock monitoring: the case of the 2019 Mw 4.9 Le Teil earthquake*, https://doi.org/10.5281/zenodo.10581351

Comments and questions are welcomed. Please contact the first author (Martijn van den Ende) via email (martijn.vandenende@oca.eu) or via Twitter (@martijnende)

Distributed Acoustic Sensing for aftershock monitoring: the case of the 2019 M_w 4.9 Le Teil earthquake

Martijn van den Ende * [1], **Jean-Paul Ampuero** [1], **Françoise Courboulex** [1], **Bertrand Delouis** [1], **Maxime Godano** [1], **Christophe Larroque** [1,2], **Anthony Sladen** [1]

[1]Université Côte d'Azur, CNRS, IRD, Observatoire de la Côte d'Azur, Géoazur, France, [2]Université de Reims Champagne-Ardenne, GEGENAA, Reims, France

Author contributions: *Conceptualization*: All authors. *Formal Analysis*: Martijn van den Ende. *Resources*: Anthony Sladen. *Writing - original draft*: Martijn van den Ende. *Writing - Review & Editing*: All authors.

Abstract Recent developments in Distributed Acoustic Sensing (DAS) have greatly expanded our capabilities for dense geophysical instrumentation by tapping into existing (but unused) fibre-optic telecommunication networks. Leveraging these so-called "dark fibres" permits an extremely rapid deployment of thousands of vibration sensors over distances of several tens of kilometres, which is ideal for rapid postseismic response efforts. Here we report on the use of dark-fibre DAS for monitoring of the aftershock sequence of the 2019-11-11 M_w 4.9 Le Teil, France earthquake. Through comparison with the local seismometer network, we assess the capabilities of the DAS array to detect and locate small-magnitude seismic events. Likely owing to cable deployment and DAS sensing characteristics, we find that the DAS noise floor is up to 3 orders of magnitude higher than that of nearby seismometers, which greatly inhibits the detection and analysis of the low-energy events. However, locating a selected aftershock with DAS yields an accuracy and precision that is comparable to that of the seismic network, even though the DAS array has a relatively unfavourable geometry. Based on these observations we provide a number of recommendations for routinely incorporating DAS into postseismic response protocols, and for optimal use of DAS alongside conventional seismic instrumentation.

Non-technical summary Recently, breakthrough technical developments have been made that allows one to use telecommunication cables as sensitive antennas recording vibrations in the earth. This technology, called Distributed Acoustic Sensing (DAS), can be used to record aftershocks that follow a large mainshock earthquake. In this work we showcase an example of using DAS for the purpose of aftershock monitoring. We first analyse the sensitivity of the technology, which is important for detecting small earthquakes. We then analyse one detected aftershock and evaluate the accuracy with which we can locate its origin location (hypocentre). Based on our findings, we

*Corresponding author: martijn.vandenende@oca.eu

provide a list of recommendations for the use of DAS in aftershock monitoring, and how to be more prepared for future earthquakes.

Résumé Les dernières évolutions en matière de Distributed Acoustic Sensing (DAS) ont considérablement accru nos capacités d'instrumentation géophysique dense grâce à l'exploitation des réseaux de télécommunication à fibres optiques existants. L'utilisation « fibres noires » permet une exploitation extrêmement rapide de milliers de capteurs de vibrations sur des distances de plusieurs dizaines de kilomètres, ce qui peut faciliter des interventions post-sismiques rapides. Nous présentons ici un rapport sur l'utilisation de dark-fibre DAS pour la surveillance de la séquence de répliques du séisme M_w 4.9 de 2019-11-11 du Teil, France. En effectuant une comparaison avec le réseau local de sismomètres, nous évaluons les capacités du réseau DAS à détecter et à localiser les événements sismiques de faible magnitude. En raison de la réduction du couplage de câble au sol et des budgets optiques, nous constatons que le niveau de bruit du DAS est jusqu'à trois ordres de grandeur plus élevé que celui des sismomètres proches, ce qui entrave considérablement la détection et l'analyse des événements de faible amplitude. Cependant, la localisation d'une réplique sélectionnée avec le DAS donne une exactitude et une précision comparables à celles du réseau sismique, bien que ce réseau DAS ait une géométrie relativement défavorable. A partir de ces observations, nous fournissons quelques recommandations pour l'incorporation systématique du DAS dans les protocoles de réponse post-sismique, et pour une utilisation optimale du DAS aux côtés des instruments sismiques conventionnels.

1 Overview

Aftershock monitoring is an essential task for communicating the evolving seismic hazard following a major (mainshock) earthquake. To inform the general public, media, urban search & rescue members, and government decision makers, seismological agencies may release aftershock forecasts that provide an expectation of the ground shaking in the affected region (Reasenberg and Jones, 1989; Becker et al., 2020; Michael et al., 2020; Calais et al., 2022). These operational forecasts can be continuously updated over time, reflecting reduced seismic hazard as the aftershock intensity subsides or increased statistical confidence as more events are being registered. Moreover, precisely located aftershocks and microseismicity illuminate fault structures that may have been previously unrecognised. Continuous monitoring of surface ground motions and registering aftershock events into preliminary catalogues is therefore of first-order importance. However, considering that the region affected by aftershocks is potentially a disaster area, one may face a number of practical challenges: power and communication line disruptions could prevent access to seismic data, individual seismic station may no longer be operational, and severely damaged infrastructure could inhibit rapid response campaigns to deploy new instrumentation. Moreover, pre-existing instrumentation may be sparse owing to inadequate seismic awareness (e.g., no recorded history of damaging seismic events), regional inaccessibility, or political instability and lack of funding. In turn, the sparsity of instrumentation and seismic data

negatively impacts the confidence bounds on aftershock forecasts, which is a necessary aspect of hazard communication (Michael et al., 2020; Schneider et al., 2022).

While not being completely immune to the challenges mentioned above, *Distributed Acoustic Sensing* (DAS; Hartog, 2017) may provide a solution in many scenarios for which conventional seismic instrumentation strategies fall short. As a subcategory of fibre-optic sensing, DAS is an interferometric technology that uses optical glass fibre cables to make continuous measurements of strain at fixed positions along the length of the fibre. With DAS, one can convert a conventional fibre-optic telecommunication cable into a dense array of equally-spaced vibration sensors. Moreover, DAS exhibits many characteristics that are highly favourable for earthquake seismology: commercially-available DAS recording instruments ("interrogators") have a sensing range of more than $100\ \mathrm{km}$ (up to $1000\ \mathrm{km}$ with state-of-the-art technology; Ip et al., 2022), and a resolution down to several metres in space and up to several kHz in time. Moreover, fibre-optic cables are highly robust and require no electrical current, and the measurement itself is single-ended, i.e., no closed-loop circuit needs to be constructed. Even when local network and vehicular traffic infrastructures are severely disrupted, part of the fibre-optic telecommunication network may still be available to DAS.

These advantages over conventional seismic instrumentation mark DAS as a potentially valuable technology for aftershock monitoring and rapid response campaigns. DAS has already been used to detect and analyse local seismic events of various magnitudes (Jousset et al., 2018; Wang et al., 2018; Sladen et al., 2019; Ide et al., 2021; Luo et al., 2021). Specifically for rapid response aftershock monitoring, Li et al. (2021) clearly demonstrated the value of even a modestly-sized DAS array located within the epicentral zone of the 2019 M_w 7.1 Ridgecrest event; by applying a template matching algorithm on three-months' worth of DAS data, these authors were able to detect 6 times more aftershocks than recorded in the standard catalogue. Furthermore, the installation of the DAS interrogator was completed within 4 days after the mainshock, highlighting the potentially short response time of DAS.

In this study, we present another case of DAS-based aftershock monitoring, following a somewhat unusual mainshock: the 2019-11-11 M_w 4.9 Le Teil, France, earthquake. Given the overall low seismicity rate in this region of France and its proximity to safety-critical infrastructure (nuclear power plants), this event was of great societal significance. Moreover, this mainshock triggered relatively few detectable aftershocks (88 events within two months), the largest of which had a local magnitude of 2.65. This situation is therefore markedly different from the scenario that was studied by Li et al. (2021), who detected $133{,}453$ events up to magnitude 5 over three months. In the present work, we discuss several aspects relevant for DAS-based aftershock monitoring, including detectability thresholds, template matching performance, and hypocentre localisation, in the context of this earthquake. We find overall that in this DAS campaign the noise floor was prohibitively high for the detection of events below magnitude 1 (in comparison to the seismometer network). Even with a conventional template matching procedure applied to the DAS data, no new events were detected. However, in spite of the unfavourable geometry of the DAS array compared to the event hypocentre, a Bayesian hypocentre inversion method applied to the DAS array and the seismometer network yielded a satisfactory hypocentre location with verified confidence bounds. In line with these results, and considering the larger perspective of rapid postseismic response, we propose several recommendations to improve preparedness by integrating DAS in rapid response protocols.

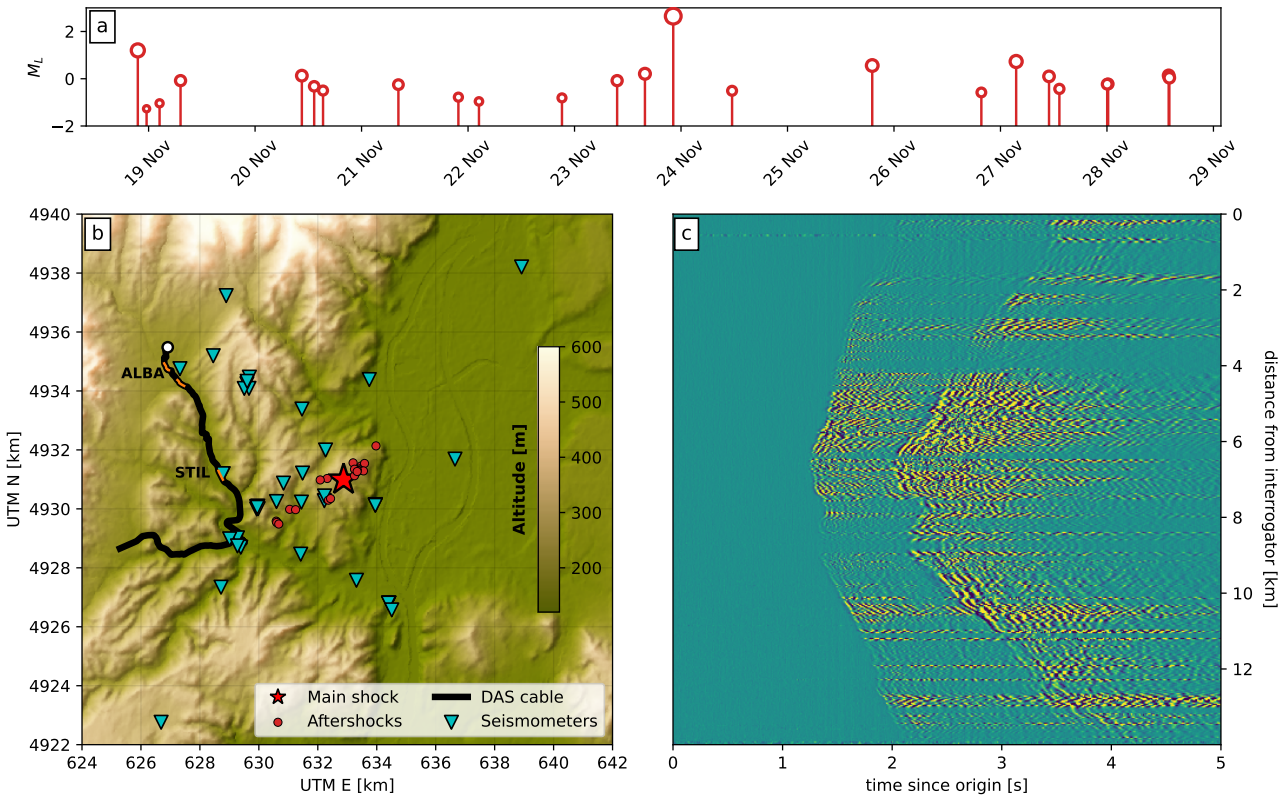

Figure 1 Overview of the Le Teil aftershock sequence. (a) Temporal distribution of aftershocks, as detected by the seismometer network (during the period of the DAS campaign); (b) Map view of the Le Teil mainshock, its aftershocks, the seismic network, and the DAS array. The DAS interrogator is placed at the northern end of the cable (at the white dot). The highlighted orange segments (3x) along the DAS array are shown in detail in Fig. 2; (c) Waterfall plot of the principal aftershock (M_L 2.65, 2019-11-23 22:14:54 UTC) recorded by DAS.

2 The 2019 M_w 4.9 Le Teil earthquake and its seismotectonic setting

As aforementioned, the Le Teil earthquake was rather unusual in several respects. This moderately-sized event was located in an area of low instrumental seismicity (Larroque et al., 2022), occurred at a very shallow focal depth between 1-2 km (Delouis et al., 2022; Vallage et al., 2021), and triggered exceptional levels of ground acceleration exceeding 1 g (Causse et al., 2021) with an almost continuous surface offset of about 10 cm over 4.5 km along strike the La Rouvière fault (Ritz et al., 2020). Situated within a epicentral radius of 60 km are 3 operational nuclear power plants and 4 major dams that control the flow of the Rhône river, underlining the societal relevance of anticipating the occurrence of similar seismic events in this fault system.

The Le Teil earthquake resulted from the reactivation of part of the La Rouvière fault (Ritz et al., 2020). This 10-km long fault is a segment of the NE-SW 120-km long Cévennes fault system that currently separates the Massif Central (a Paleozoic basement domain) from the South-East basin of France (a Meso-Cenozoic sedimentary domain) from Montpellier to Valence (Suppl. Fig. S1). The Cévennes fault system is a major structural boundary that experienced several periods of activity since Paleozoic times, the last one corresponding to normal faulting during the Oligocene (Roure et al., 1992; Bonijoly et al., 1996; Ritz et al., 2020; Marconato et al., 2022).

3 Data acquisition

Immediately following the Le Teil mainshock, temporary deployment efforts were mounted to capture the aftershock sequence; the details of this rapid response are described in Cornou et al. (2021), and an overview of the campaign is given in Fig. 1. In addition to the installation of nodal seismometers, a Febus A1-R DAS interrogator (provided by Febus Optics) was connected to a fibre-optic cable belonging to the commercial telecom network of Orange. The interrogator was installed in the village of Alba-la-Romaine (northernmost point of the cable, at the white dot in Fig. 1b), and the cable was sensed over a total distance of $14\ \mathrm{km}$ up to the village of Valvignières (westernmost point of the cable in Fig. 1b). The DAS data were recorded at a spatial resolution (gauge length and channel spacing) of $3.2\ \mathrm{m}$, which was subsequently downsampled to $9.6\ \mathrm{m}$, and sampled in time at a rate of $400\ \mathrm{Hz}$. The installation of the DAS system was completed on 2019-11-18, and acquisition continued until 2019-11-28. During this period, 25 aftershocks were registered by the seismometer network (see Fig. 1a). The largest aftershock of local magnitude 2.65 was recorded by DAS on 2019-11-23 22:14:54 UTC, which we refer to as the *principal aftershock*. Owing to the high quality of the recordings, we use this event to illustrate certain concepts relevant for DAS-based aftershock monitoring.

For the majority of its trajectory the DAS cable follows a major road, and hence the seismic and quasi-static signals of vehicles are abundant in the data (see van den Ende et al., 2022). The location of the cable was determined based on documentation provided by the operator, and an a-posteriori calibration procedure based on these traffic signals. Unfortunately, the internal clock of the interrogator could not be synchronised with a time base in common with the seismometers; instead, a relatively imprecise network time protocol was used to timestamp the data. For the localisation of the principal aftershock (Section 6), for which absolute times are critical, we estimate the absolute time error by comparing seismic phase arrivals at the DAS cable and a nearby seismometer. Specifically, station 3C.STIL was positioned within $100\ \mathrm{m}$ from the cable (see Fig. 2b), and by comparison of the two sets of recordings of the principal aftershock we estimated the time delay to be $0.307\ \mathrm{s}$.

The 3C seismometer network (Bertrand et al., 2019) comprises a mix of predominantly Guralp CMG-6T broadband and Fairfield ZLand nodal seismometers, which were deployed shortly after the mainshock. Supplementary Table S4 lists the stations used in this study, their locations, and the phase picks for the principal aftershock.

4 Detectability and signal-to-noise

In principle, DAS exhibits a sensitivity that can be comparable to high-gain seismic stations (Lior et al., 2021). However, this competitive sensitivity is subject to local conditions, such as the apparent phase velocity of the signal and the quality of the coupling between the optical cable and the surrounding medium. Particularly for those cables that were deployed for telecommunication purposes, the deployment conditions are often sub-optimal for earthquake seismology applications. Moreover, the ambient seismic noise may vary dramatically depending on the cable's proximity to anthropogenic noise sources (roads, wind turbines, railways). This can be seen clearly in the DAS recordings of the principal aftershock as spatial variations in the amplitude of the wavefield (Fig. 1c).

We explore these amplitude variations in more detail by considering three segments along the DAS cable – see Fig. 1b and Fig. 2. The first segment is located in the centre of the village Alba-la-Romaine, while the second segment follows a dirt road into a vineyard at the edge of the village. Both segments are located within a few hundred metres

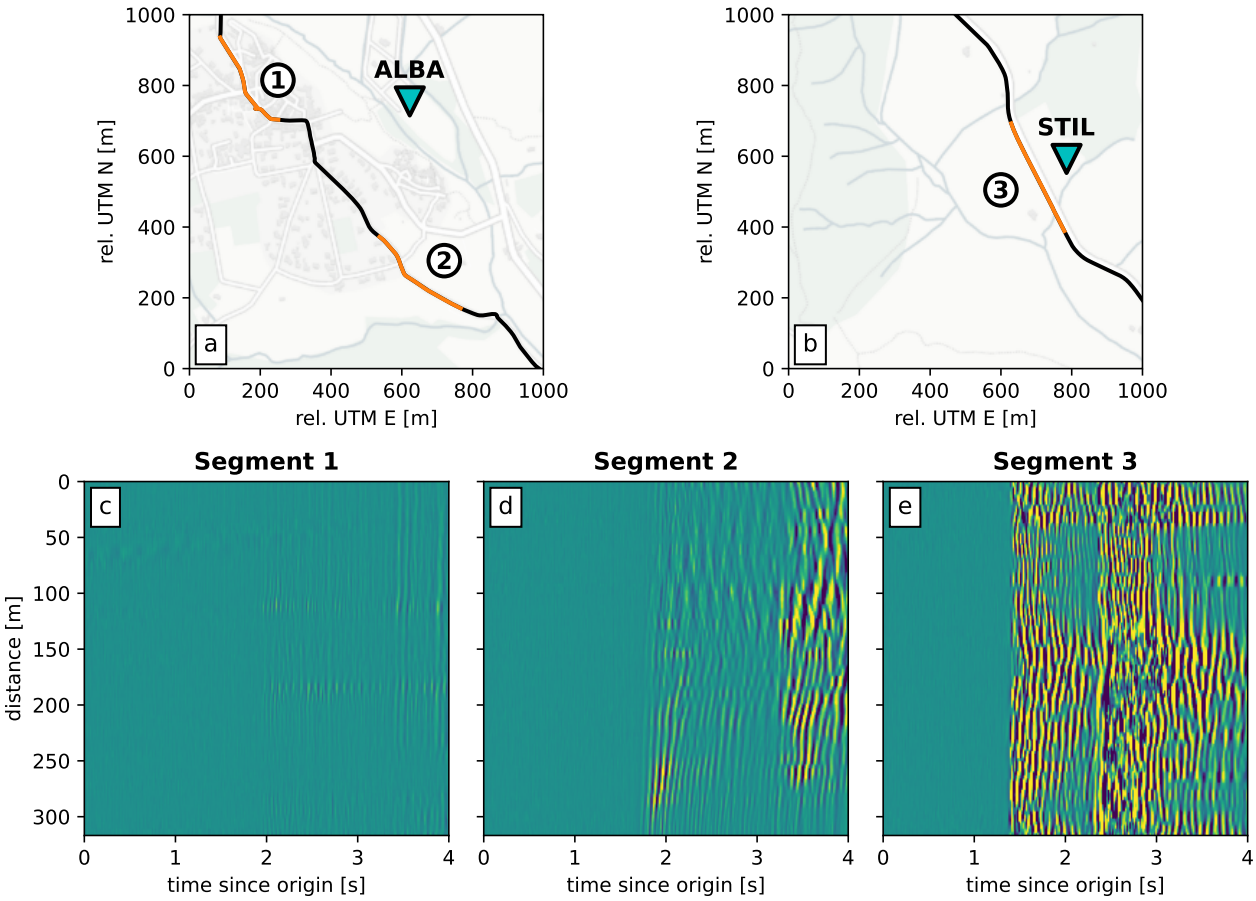

Figure 2 Detailed views for selected DAS segments. (a) Map view of segments 1 and 2, and nearby seismometer ALBA; (b) Map view of segment 3 and nearby seismometer STIL; (c-e) The principal aftershock recorded by the selected segments (identical colour scale).

from the ALBA station. The third segment is located along a major road connecting Alba-la-Romaine with Saint-Thomé, positioned within 100 m from the STIL station. By comparing the amplitudes of the recorded wavefield for each of these segments (Fig. 2c-e), one could conclude that Segment 3 is particularly well suited for the detection and analysis of (small) aftershocks. However, owing to the favourable proximity of this segment to the seismic source on the one hand, and the potentially unfavourable ambient noise environment, this conclusion may be too preliminary.

For a better comparison between the different DAS segments, we make use of the nearby seismometers. Firstly, we convert the DAS strain rate recordings $\dot{\varepsilon}$ into equivalent acceleration $\ddot{u}$ using the relationship $\ddot{u} = c\dot{\varepsilon}$ (Daley et al., 2016), with c being the apparent phase velocity (here taken to be 3 km s^{-1}, which corresponds approximately with the apparent wave speed of the most energetic phase). The particle velocity recordings of ALBA and STIL are converted into acceleration through time-differentiation. We then compute the acceleration spectra for the principal aftershock recordings of both types of instruments for a 20-second time window centred around the event origin time. This procedure is repeated for two additional aftershocks of lower magnitude (M_L 1.20 and M_L 0.73). To obtain a measure of the local noise floor, we compute the acceleration spectra over two 1-hour time periods, one starting at midnight and one starting at noon (local time), using Welch's method (Welch, 1967). The results of this analysis are given in Fig. 3.

Let us first consider the ambient noise spectra; given that Segment 2 is located in an area that does not experi-

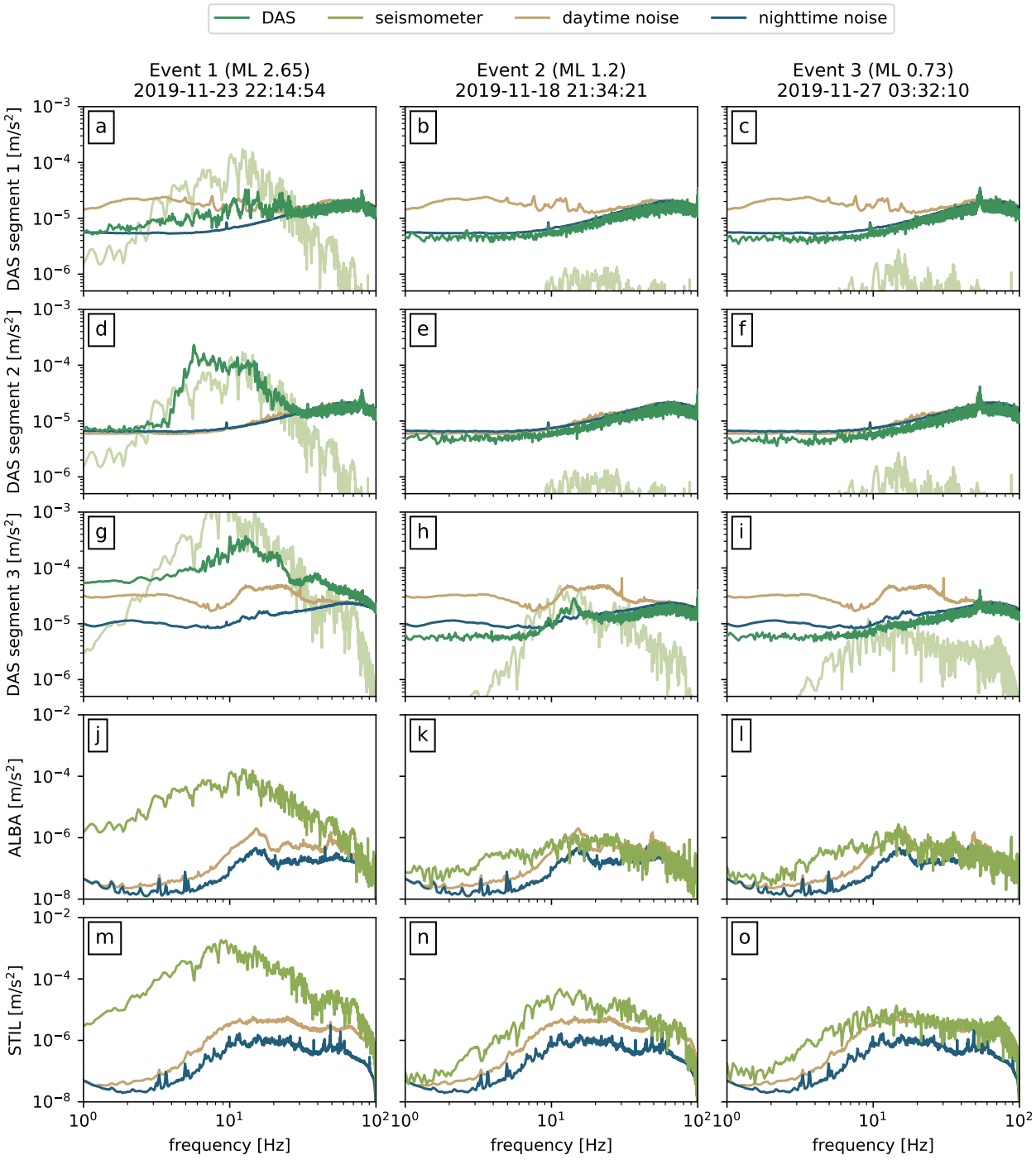

Figure 3 Spectral amplitudes of the three largest aftershocks, compared to the (local) noise floor. (a-i) DAS recordings for the three selected segments, converted to an acceleration spectrum using an average apparent phase velocity of $3\ \mathrm{km\ s^{-1}}$ and averaged over all channels in the segment. For reference the acceleration spectrum of the closest seismometer (ALBA for segments 1 and 2, STIL for segment 3) is plotted in the background; (j-o) Seismometer (ALBA and STIL) recordings converted to an acceleration spectrum through differentiation. Note that the vertical axis ranges for the DAS and seismometer panels are different to better represent the noise floor of each instrument.

ence much anthropogenic noise, the daytime and nighttime noise spectra for this segment are practically identical (Fig. 3d), being similar to the nighttime spectra of the other DAS segments (panels a and g). By contrast, the daytime spectra of these other segments are elevated by at least a factor 2, which is particularly clear towards the lower frequency of 1 Hz. The observed difference between night and day further indicates that the instrumental noise floor is at most at the nighttime noise level, and possibly much lower. Interestingly, the lower bound of the nighttime noise floor (at 10^{-5} m s^{-2}) lies well above the noise floor bounds of the seismometers (10^{-8}-10^{-6} m s^{-2}). This implies that, even though the recorded noise levels are above the instrumental noise, they are much higher for DAS than for the seismometers.

When comparing the spectra of the principal aftershock (left column of Fig. 3), there is a good agreement between Segment 2 and ALBA in the 0.3-3 Hz range. The recorded amplitudes of Segment 1 are almost one order of magnitude lower than those of Segment 2 and of ALBA, suggesting that this segment exhibits poor coupling. Segment 3 displays the largest spectral amplitudes primarily owing to its proximity to the seismic source; STIL, being closer to the seismic source, exhibits larger spectral amplitudes than ALBA, which is likely expressed at Segment 3. Overall, the DAS segments exhibit a signal-to-noise ratio (SNR) that is a factor 10 at best, compared to an SNR of up to 1000 for the seismometers. To further underline this last point, we perform similar experiments for two lower-magnitude aftershocks. For the M_L 1.20 event (middle column of Fig. 3), only Segment 3 experiences a small signal above the nighttime noise floor. The M_L 0.73 event remains well below the nighttime noise floor for all DAS segments, and slightly exceeds that of the seismometers.

5 Template matching

Given the unfavourable noise floor characteristics of the DAS array, a reasonable strategy would be to apply a template matching procedure to the DAS data. Already for many years template matching has served to detect recurring and/or low-amplitude seismic events (Gibbons and Ringdal, 2006; Shelly et al., 2007; Lengliné et al., 2016; Hutchison and Ghosh, 2019; Ross et al., 2019), even those that are potentially buried within the noise floor of conventional seismometers. Several studies have demonstrated the feasibility of template matching when applied to DAS data (Li and Zhan, 2018; Li et al., 2021; Jousset et al., 2022), hence offering an optimistic outlook to detect previously unnoticed events in this aftershock sequence.

To this end, we adopt a conventional template matching approach. We take the three selected aftershocks that were discussed in the previous section (see Supplementary Figure S2) as templates, extracting a time window of 5 seconds centred around the first arrival, and bandpass filtering the data between 5 and 30 Hz in which the SNR is optimal (see Fig. 3). We cross-correlated the templates with chunks of 60-second of DAS data filtered in the same frequency band. The (normalised) cross-correlation was performed along the time axis, and the result was averaged over the DAS channel axis, yielding three time-series of normalised cross-correlation coefficients for the entire DAS data set (one for each template). We then manually inspected the 9 occurrences for which the cross-correlation coefficient exceeded the background fluctuations above a threshold of 8×10^{-4}. From this manual inspection, we could only recognise the original templates, but not any other aftershocks. Rather, most of these detections seemed associated with high-amplitude traffic noise.

This negative result corroborates the findings of the previous section, in that the DAS noise floor seems prohibitively high for the detection of low-energy events, even with a technique as sensitive as template matching. By contrast, previous studies did report successful experiments in similar, near-field earthquake scenarios, hence raising questions regarding the performance of template matching applied to our fibre deployment. If we consider the PoroTomo experiment as studied by Li and Zhan (2018), it is clear that the local deployment conditions were much more favourable; the example given in their Fig. 1b shows the recordings of a magnitude -0.5 event which clearly exceeds the noise level, even at such low source magnitude. The dedicated deployment of this DAS array, which was not a commercial dark fibre, and its proximity to the seismic source area were greatly beneficial. A more similar scenario to ours is that presented by Li et al. (2021), who examined the Ridgecrest aftershock sequence with a dark-fibre DAS array at an epicentral distance in the range of 10-20 km. With template matching applied to the DAS data, they registered over 6 times more events than present in the standard SCSN catalogue (Hauksson et al., 2020). However, they did note a similar performance gain was obtained when applying template matching to the conventional seismometer network in the region (Shelly, 2020), and so the enhanced cataloguing abilities are more attributable to the characteristics of template matching than to the characteristics of DAS. In our case, the aftershock catalogue was obtained with template matching applied to the (dense) seismic network in the epicentral area, hence only modest improvements could be expected at best. But considering the relatively high noise level of the DAS recordings compared to the seismometers, it becomes clear why the seismic network was able to detect more events than the DAS array (using template matching).

6 Hypocentre inversion

Aside from seismic event detection, locating the detected events is a critical task for aftershock monitoring. In this section, we will discuss and implement a Bayesian hypocentre inversion protocol, and apply it to a combination of DAS and seismometer data to assess the feasibility of using DAS for event localisation efforts. Subsequently, we compare the extent of the posterior distributions with the confidence interval resulting from uncertainty in the phase picks. In the present scenario, the velocity model is sufficiently simple to permit such a direct comparison, and from which we can draw more general conclusions.

6.1 Stein Variational Inference

Recently, Smith et al. (2022) proposed a Bayesian hypocentre inversion approach based on the minimisation of a kernelised Stein discrepancy, called Stein Variational Inference (SVI) (Liu and Wang, 2016). This mesh-free gradient-descent algorithm provides a computationally cheap estimation of the posterior distribution of an optimisation problem by invoking a finite number of "particles" that represent candidate solutions in the problem's parameter space. The dynamics of these particles are governed by the gradients of the solution manifold, attracting the particles towards minima on the manifold. To prevent collapse onto the maximum-likelihood solution (or into other minima), the particles repel one another based on their mutual spacing. Upon convergence of the algorithm, the equilibrium positions of the particles delineate the posterior distribution of the hypocentre location. In the following section, we will briefly describe the SVI method and highlight a few aspects that are implicit in the work of Liu and Wang (2016). We aim to provide a description that is sufficiently precise, yet matching the simple intuition discussed above; for a

rigorous mathematical treatment, see Liu and Wang (2016).

To start, let $\{\mathbf{x}_n\}_{n=1}^{N}$ denote a set of particles representing candidate hypocentres $\mathbf{x} \sim \mathcal{X} \in \mathbb{R}^3$. These particles are randomly initialised at step $\ell = 0$. The target distribution that the particles will eventually approximate is characterised a probability density function $\rho(\mathbf{x})$. Finally, let $\kappa(\cdot,\cdot) : \mathcal{X} \times \mathcal{X} \to \mathbb{R}^1$ denote a positive definite kernel, such as the Radial Basis Function (RBF) or Laplacian kernel. The locations of the particles in the solution space are then updated through a gradient-descent step as:

$$\mathbf{x}_n^{\ell+1} = \mathbf{x}_n^{\ell} + \eta^{\ell}\phi\left(\mathbf{x}_n^{\ell}\right), \tag{1}$$

with η^{ℓ} denoting the step size at step ℓ, and with $\phi : \mathcal{X} \to \mathbb{R}^3$ defined as:

$$\phi\left(\mathbf{x}_n\right) = \frac{1}{N}\sum_{i=1}^{N} \underbrace{\kappa\left(\mathbf{x}_n, \mathbf{x}_i\right)\nabla_{\mathbf{x}_i}\log\rho\left(\mathbf{x}_i\right)}_{\text{attractive force}} + \underbrace{\nabla_{\mathbf{x}_i}\kappa\left(\mathbf{x}_n, \mathbf{x}_i\right)}_{\text{repulsive force}} \tag{2}$$

As highlighted above, this expression for ϕ reveals an interplay between two opposing forces: the first term attracts the particles towards a (local) minimum of ρ, for which $\nabla_{\mathbf{x}_i}\log\rho\left(\mathbf{x}_i\right)$ is zero. This collapse onto the minimum is prevented by a repulsive term given by $\nabla_{\mathbf{x}_i}\kappa\left(\mathbf{x}_n, \mathbf{x}_i\right)$, which is positive non-zero for $\mathbf{x}_n \neq \mathbf{x}_i$.

At this point, the functional form of ρ is not yet specified. To obtain a proper posterior distribution $p\left(\mathbf{x} \mid \{t\}\right)$, one takes Bayes' rule $\rho(\mathbf{x}) = p\left(\mathbf{x} \mid \{t\}\right) \propto p\left(\{t\} \mid \mathbf{x}\right) q\left(\mathbf{x}\right)$, with $p\left(\{t\} \mid \mathbf{x}\right)$ denoting the likelihood of observing a set $\{t_i\}_{i=0}^{T}$ arrival times given hypocentre $\mathbf{x}$, and $q\left(\mathbf{x}\right)$ denoting the prior probability of $\mathbf{x}$. Writing out Eq. (2) in full then gives:

$$\phi\left(\mathbf{x}_n\right) = \frac{1}{N}\sum_{i=1}^{N} \underbrace{\kappa\left(\mathbf{x}_n, \mathbf{x}_i\right)\nabla_{\mathbf{x}_i}\log p\left(\{t\} \mid \mathbf{x}_i\right)}_{\text{attraction towards likelihood}} + \underbrace{\kappa\left(\mathbf{x}_n, \mathbf{x}_i\right)\nabla_{\mathbf{x}_i}\log q\left(\mathbf{x}_i\right)}_{\text{attraction towards prior}} + \underbrace{\nabla_{\mathbf{x}_i}\kappa\left(\mathbf{x}_n, \mathbf{x}_i\right)}_{\text{repulsion}} \tag{3}$$

For a uniform ("flat") prior distribution $\nabla_{\mathbf{x}}\log q\left(\mathbf{x}\right) = 0$, so that the particle distribution settles around minima in the likelihood distribution.

The gradient stepping scheme (Eq. (1)) can be solved by conventional gradient descent algorithms, as long as $\rho\left(\mathbf{x}\right)$ is differentiable with respect to $\mathbf{x}$. This in turn requires that the forward model generating synthetic phase arrivals $\{\tau\} = F\left(\mathbf{x} \mid \mathcal{M}\right)$ given a velocity model $\mathcal{M}$, be differentiable. Smith et al. (2022) addressed this for a three-dimensional velocity model by parameterising $F\left(\mathbf{x} \mid \mathcal{M}\right)$ with a Neural Network $N\left(\mathbf{x}\right) \approx F\left(\mathbf{x} \mid \mathcal{M}\right)$, which is differentiable by design. The downside of letting a Neural Network represent the forward calculation, is that it requires re-training for each new velocity model, nor does it provide any guarantees on the physical validity of the solution. Fortunately, Eikonal solvers and many ray tracing algorithms are in principle differentiable (see Rawlinson et al., 2008), permitting one to use conventional seismological tools in conjunction with the SVI framework.

Lastly, we note that one must exercise caution in the choice of the gradient descent algorithm; as aforementioned, the SVI particle distribution will settle around minima in the target distribution. The classical gradient descent algorithm potentially converges to local minima, whereas algorithms that include a momentum term (such as the Adam algorithm; Kingma and Ba, 2017) may escape these local minima to converge towards the global minimum (or another strong attractor). This behaviour may not always be desired, since in that case the particle distribution will no

longer accurately reflect the full posterior distribution. For potentially multi-modal posterior distributions (which are conceivable for complex 3D velocity structures), a momentum-free optimiser should be preferred.

6.2 Inversion procedure

For locating the hypocentre of the principal aftershock, we manually picked the P and S-phase arrivals recorded by the seismic stations listed in Supplementary Table S4. The same phases were picked on the DAS array, picking 1 out of 100 channels (evenly distributed along the cable; see Supplementary Figure S3). This resulted in a set of observations $\{t\}$ consisting of respectively 42 and 41 P and S-picks for the seismometers, and 43 P and S-picks for the DAS array.

We adopted the Equal Differential Time (EDT) formulation (Lomax et al., 2000; Font et al., 2004) to compute the likelihood distribution, given by:

$$p\left(\{t\} \mid \mathbf{x}\right) \propto \exp\left(-\frac{1}{N_t^2}\sum_{i,j}^{N_t}\left[\frac{\Delta t_{ij} - \Delta\tau_{ij}}{\sqrt{2}\sigma}\right]^2\right) \tag{4}$$

For N_t arrival time observations in the set $\{t_i\}_{i=1}^{N_t}$, and $\{\tau_i\}_{i=1}^{N_t}$ synthetic arrival times at the same receiver locations, the differential times are defined as $\Delta t_{ij} = t_i - t_j$ and $\Delta\tau_{ij} = \tau_i - \tau_j$. The uncertainty in the data is expressed by σ, which we set to 0.1 s (an order-of-magnitude estimation of the picking uncertainty). One of the advantages of the EDT method is that it does not require both P and S phase arrivals to be recorded at a given receiver. Since DAS is more sensitive to S-phases than to P-phases, being able to discern P and S-phases everywhere along the DAS array is a luxury reserved only for high SNR recordings. Moreover, for large N_t, $p\left(\{t\} \mid \mathbf{x}\right)$ can be approximated stochastically by randomly drawing observations from $\{t\}$, rather than computing Δt_{ij} for all combinations of i and j. This stochastic SVI inversion approach is equivalent to stochastic gradient descent used in Deep Learning. In the present study, the number of observations is limited, but when $N_t \gg 1000$ (for instance when applying an automated phase picker to a DAS array with $10{,}000$ sensors), it is computationally beneficial to approximate p stochastically. Note also that we compute the mean over N_t^2 differential times instead of their sum, which is essential for a proper balancing between the various terms in (3); when using a sum operation, the particle distribution contracts proportional to the number of observations, resulting in a strong underestimation of the uncertainty with increasing N_t.

The velocity model adopted here is modified from Delouis et al. (2022): $v^p = a + bz = 4.5 + 0.07z$ [km s^{-1}] with a v^p/v^s-ratio of 1.9 and the absolute depth z being measured positive down. An alternative velocity model proposed by Causse et al. (2021) was found to give an unsatisfactory fit with the wavefield recorded by DAS (see Supplementary Figure S3). The one-dimensional, constant velocity gradient model permits an analytical solution for the synthetic arrival times at sensor $\mathbf{s}_i$ (Cerveny, 2001):

$$\tau_i = F\left(\mathbf{x}, \mathbf{s}_i\right) = b^{-1}\arccos\left(1 + \frac{b^2 r_i^2}{2v_{\mathbf{s}}v_{\mathbf{x}}}\right), \tag{5}$$

with r_i denoting the Euclidean distance between $\mathbf{x}$ and $\mathbf{s}_i$, $v_{\mathbf{s}}$ the phase velocity at $\mathbf{s}$, and $v_{\mathbf{x}}$ at $\mathbf{x}$ (either for v^p or v^s). As can be seen in Fig. 1b, the local topography is significant compared to the hypocentral depth, and so we define $z = 0$ at nominal sea level and include the receiver altitude in the calculation of r_i and $v_{\mathbf{s}}$. We adopt the Radial Basis

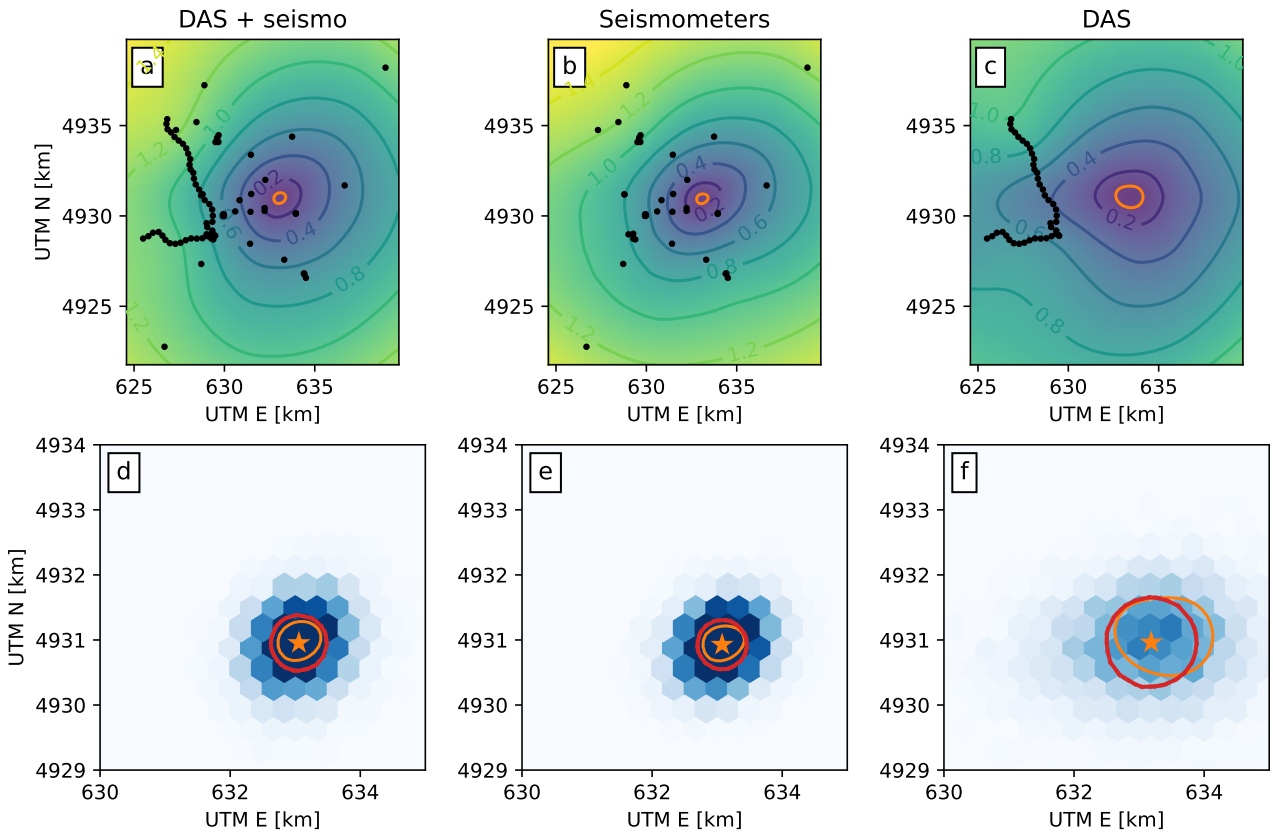

Figure 4 Visualisation of the principal aftershock hypocentre location uncertainty. (a-c) Location uncertainty expressed in absolute arrival time residuals when using the DAS array and seismometer network, only the seismometer network, or only the DAS array. Each contour line represents an increment in the mean residuals of 0.2 s. The contour line highlighted in orange represents an uncertainty of 0.1 s. The location of the seismic receivers (DAS or seismometers) are indicated in black; (d-f) SVI particle density computed over an hexagonal grid, for the same three instrumentation sets as for a-c. The median of the particle cloud is indicated by the orange star, and the 0.1 s contour line as shown in a-c is re-plotted here. For comparison, the convex hull of the particles that fall within a 1σ-distance from the hypocentre is indicated in red.

Function as a convenient positive definite kernel:

$$\kappa\left(\mathbf{x}_n, \mathbf{x}_i\right) = \exp\left(-\frac{1}{h}||\mathbf{x}_n - \mathbf{x}_i||_2^2\right) \tag{6}$$

The scaling parameter h is computed as $h = \text{med}^2 / \log N$ (med denoting the median Euclidean distance between the particles), which dynamically balances the attractive and repulsive forces in Eq. (3) (Liu and Wang, 2016). $N = 5000$ particles are initialised uniformly within the region, and the SVI algorithm is iterated to convergence over 1000 steps.

6.3 Uncertainty quantification and performance

To evaluate the contribution of the DAS array to locating the hypocentre of the principal aftershock, we apply the above procedure individually to the DAS array, the seismometer network, and both combined. In the case of a monotonic, one-dimensional velocity model, the solution manifold is smooth and close to convex, meaning that there are no strong attractors (local minima, ridges, or saddle points) other than the global minimum corresponding with the maximum likelihood. We can clearly see this in Fig. 4 a-c, which shows the median absolute residuals for different epicentre locations. In accordance with $\sigma = 0.1$ s, we delineate the 0.1 second-contour of these residuals in orange. When using only data from the DAS array, the radius of this contour is around 1 km, whereas when using only data

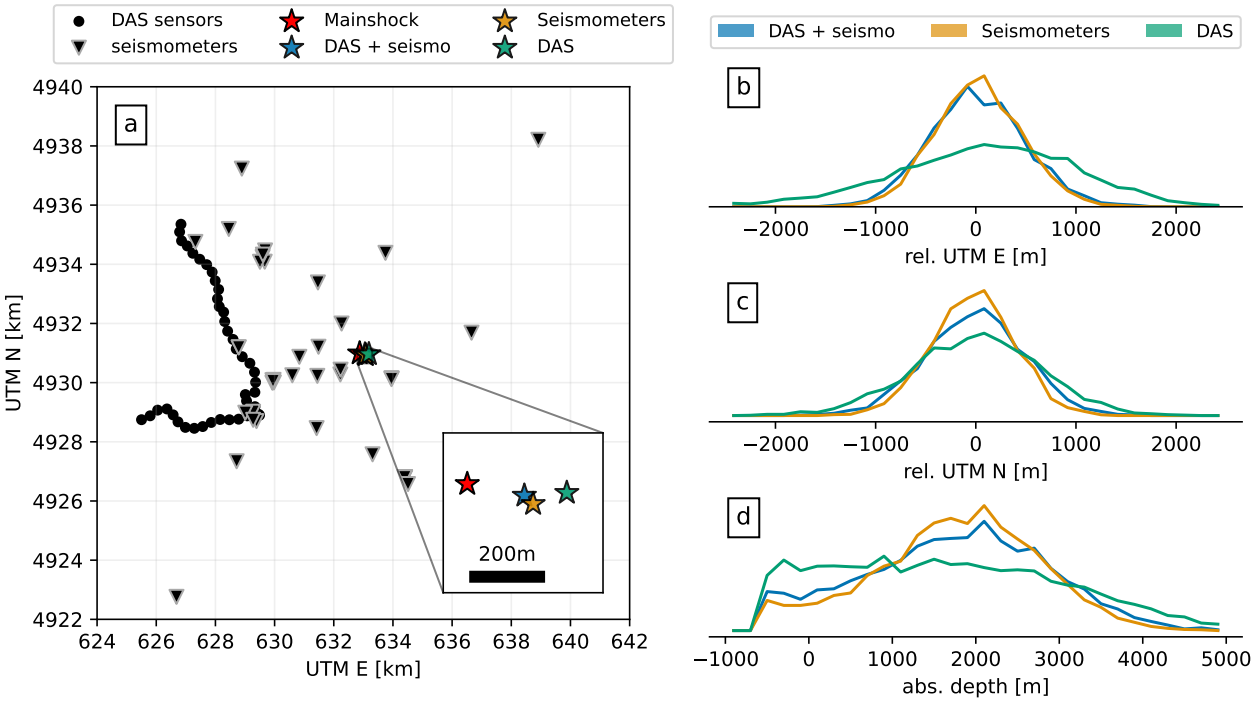

Figure 5 Results for the inversion of the principal aftershock. (a) Map view of the epicentre of the Le Teil mainshock (not inverted for), and the principal aftershock epicentre estimates when using only DAS, only seismometers, or both combined; (b-c) Histograms of the estimated posterior distributions of the epicentre coordinates, relative to the median estimate, for each type of instrumentation. The median estimates are given in Table 1; (d) Histograms of the estimated posterior distributions of the hypocentral depth (relative to nominal sea level), for each type of instrumentation.

from the seismometer array, the radius of this confidence interval shrinks to roughly 300 m. Given the relatively unfavourable geometry of the DAS array compared to the seismometer network, the increased uncertainty in the epicentre location is not surprising. Nonetheless, DAS array alone provides a satisfactory epicentre location, with its confidence interval overlapping with the inversions including the seismometers.

Since the prior distribution is taken to be uniform, we expect the SVI particle distribution to concentrate within the 0.1 second contour interval, with its median coinciding with the maximum likelihood hypocentre location. To visualise the particle distribution accurately, instead of plotting the point cloud directly (which draws the attention to outliers), we represented the posterior distribution in Fig. 4 d-f as the particle count density on a hexagonal grid. As expected, the highest density of particles coincides within the 0.1 s confidence intervals. Quantitatively, when computing the 68 % confidence intervals around the median of the particle distribution (equivalent to ± 1 standard deviation for a Gaussian distribution), we find that these are comparable in magnitude to the extent of the 0.1 s contours – this is indicated by the red contour in Fig. 4 d-f and in Table 1. We therefore conclude that the SVI inversion procedure, including the dynamic computation of the scaling factor h, yields an accurate representation of the pos-

Input data	rel. UTM E [m]	rel. UTM N [m]	Depth [m]
Only DAS	186 ± 898	62 ± 634	1552 ± 1522
Only seismometers	76 ± 431	28 ± 414	1827 ± 989
DAS + seismometers	57 ± 469	54 ± 487	1792 ± 1164

Table 1 Results for the inversion of the principal aftershock. The location is given in UTM coordinates (zone 31T) relative to [633 km E, 4930.9 km N]. The location uncertainty is estimated as the 68 % confidence interval around the median estimate (see Fig. 5).

terior distribution. This is highly desirable, for otherwise manual tuning of a constant h would affect the extent of the posterior distribution (Smith et al., 2022), and its interpretation in terms of location uncertainties.

7 Perspectives for rapid postseismic response

Considering the observations made in the previous sections, an ambivalent picture emerges: on the one hand, the dark-fibre DAS array under investigation exhibited a greatly elevated noise floor (as compared to nearby seismometers). The legacy model instrument that was rapidly provided by Febus Optics for this experiment, may not have performed up to similar levels as their current flagship models. But considering that day-night variations in the background noise can be clearly observed, it is unlikely that these elevated noise levels can be attributed solely to instrumental noise; instead, deployment characteristics and the DAS measurement principle itself should be considered. It is well known that strain measurements have an increased sensitivity to slowly propagating phases such as surface waves (Daley et al., 2016; van den Ende and Ampuero, 2021), which contribute negatively to the signal quality. As such, DAS holds a disadvantage compared to seismometers in "noisy" (urban or coastal) environments. Moreover, local deployment conditions (notably cable-ground coupling) affect the strain amplitudes that can be recorded and therefore the ratio of seismic amplitudes (earthquake signal or ambient noise) to instrumental noise amplitudes. As a result, the ability to detect (small) seismic events with DAS is diminished. Even with a sensitive detection method like template matching, very few aftershocks of the Le Teil mainshock could be detected with DAS. We do note that this aftershock sequence is noticeably less productive than a "classical" aftershock sequence, in that only 88 events were catalogued over two months (using the seismic network), out of which 25 occurred during the DAS experiment. By comparison, the 1996 M_L 5.3 Epagny event, which occurred in a similar geological context as the Le Teil earthquake, produced over 400 detectable aftershocks (Thouvenot et al., 1998). Moreover, the maximum magnitude of the Le Teil aftershocks were well below the expectation from Bath's law (expected maximum magnitude: 3.7; observed: 2.7). In the case of a more productive aftershock sequence, both in terms of the event magnitude and occurrence rate, it is likely that many more events would have been registered by the DAS array. Moreover, aftershock catalogues are typically created with energy detectors (like STA/LTA), which tend to be less sensitive than template matching. Hence, a comparison between a DAS-based template matching catalogue and a conventional seismometer-based catalogue would obfuscate the DAS detectability issues to an extent. The case of the Le Teil aftershock sequence makes the contrast between the performance characteristics of the DAS array and the seismic network strikingly clear.

On the other hand, events that DAS records with a sufficient signal-to-noise ratio can be located with reasonable accuracy and precision using only a DAS array, even if the geometry of the cable route is not optimal (e.g. poor azimuthal coverage as seen in Fig. 4). In the present study, the network of seismometers was very dense and well-positioned around the epicentral area, rendering the contribution from the DAS array inconsequential, but this cannot be expected in general: in regions with reduced accessibility (mountainous, forested, or off-shore environments) the deployment of a dense, azimuthally-encompassing seismometer network is an enormous challenge. In such scenarios, a single DAS array likely has to operate independently to locate seismic events, which we found to be feasible.

In terms of rapid postseismic response, there are various strategies that can be adopted. The seismological community at large is currently at a stage of *reactive* response: when a significant mainshock earthquake occurs, in-

dividual research teams seek access to a suitable dark fibre in the area and install their equipment as soon as the access is granted. As the Ridgecrest and Le Teil experiments have demonstrated, the effective response time for a DAS deployment is at least several days, which is comparable to that of temporary seismometer deployment efforts in well-accessible areas. However, in contrast to seismometer deployments, DAS experiments can be prepared in advance, allowing the community to progress from a reactive to a *proactive* postseismic response. Based on the lessons learned from the Le Teil experiment, and the observations presented in this work, we make the following recommendations:

1. The precise timing of a large mainshock cannot be foreseen, but regions of elevated seismic hazard that are likely to host such events can be marked ahead of time (e.g. Danciu et al., 2021). Therefore, it is possible to identify in advance suitable sites for the deployment of a DAS array. Agreements for access to dark fibre can be struck with local operators, and possibly improvements of the local fibre network (coupling quality and optical budget) can be made in anticipation. Moreover, one could consider conducting a short-term experiment to characterise the ambient noise floor, and make a preliminary assessment of the detectability thresholds of the DAS array. After the initial preparations have been made, no maintenance or further action is required until a significant seismic event occurs, which is a benefit of DAS over conventional instrumentation.

2. Instead of relying on existing dark-fibre infrastructures, dedicated DAS arrays can be deployed at key localities in regions of high seismic activity. While the deployment itself can be costly, it allows for a greater range of optimisation to be made specifically for the purpose of earthquake monitoring: improving cable-ground coupling and cable jacketing or armouring (Dou et al., 2017; Ajo-Franklin et al., 2019), using impurity-doped fibre (Correa et al., 2017), femtosecond-laser inscription (Wu et al., 2020), and helical wounding (Kuvshinov, 2016) may contribute to an improved signal-to-instrument-noise ratio. Moreover, the geometry of the array can be designed with specific array processing techniques in mind, such as beamforming. When combined with one or more conventional seismometers, DAS strain recordings can be converted into particle motion, rendering DAS essentially equivalent to the seismometers in terms of sensitivity and detectability (see van den Ende and Ampuero, 2021; Trabattoni et al., 2023, for an in-depth discussion). Systematically deploying such single-purpose DAS arrays is only financially feasible for sizeable research consortia and institutes with dedicated financial support, but the cost-benefit ratio could be worth considering.

3. Even in the scenario in which only a dark-fibre DAS array is available, the contribution of DAS can be important when conventional instrumentation is sparse; although the event detectability of DAS may be subpar to that of seismometers, relatively large events that are well-recorded could be located using the DAS array and the remaining (few) receivers in the area. Smaller events not recorded by DAS but captured with seismometers can then be located relative to the more precisely-located reference event using double-difference methods (Waldhauser and Ellsworth, 2000). This interplay between the dense DAS array and the sensitive, conventional instrumentation leverages the advantages of both.

As demonstrated by the 2023 M_w 7.8 Kahramanmaraş, Turkey earthquake, having dense instrumentation around the epicentre of a relatively large-magnitude event is critical for revealing the seismic source processes in high reso-

lution (Delouis et al., 2023; Melgar et al., 2023). As long as no scientific and political consensus is achieved to intentionally induce an earthquake in a targeted (and instrumented) area (as proposed by Savage et al., 2017), possibly the next best solution to record a large event in high resolution is to capture the largest aftershocks of a large mainshock (e.g. an M 6 aftershock following an M 7+ mainshock). Since fortunately such large events are rare occurrences, the seismological community needs to be prepared to act swiftly, as the largest aftershocks typically occur in the earliest phase of the aftershock sequence. DAS is giving the seismological community this opportunity to be more prepared for future seismic events. By laying the groundwork to access multiple DAS arrays in an area around an anticipated epicentre, and by developing and practising rapid-response protocols, we may place ourselves in a unique position to image the seismic source of a large event with unprecedented resolution.

8 Conclusions

In this work, we analysed the performance characteristics of a dark-fibre DAS array in the context of monitoring of the aftershock sequence of the 2019-11-11 M_w 4.9 Le Teil, France earthquake. In contrast to other, well-known aftershock sequences (such as the Ridgecrest sequence), the Le Teil mainshock was followed by an anomalously low number of 88 aftershocks over a period of two months, the largest of which was of local magnitude 2.65. Over the two-week duration of the DAS experiments 25 aftershocks were recorded by the local seismometer network, only some of which being visible in the DAS data. By comparing the ambient noise and earthquake spectral amplitudes of the DAS array with those of nearby seismometers, we find that the DAS noise floor is higher than that of the seismometers by up to three orders of magnitude, greatly inhibiting the event detection performance of DAS. We note that these elevated noise levels are likely due the measurement principle of DAS and local deployment conditions, rather than due to instrumental noise. Consequently, a template matching search applied to the DAS data did not yield any new detections outside of the existing (template matching) catalogue. Events that are detectable by DAS can be located by with an accuracy and precision that is comparable to the seismometer network (about twice larger uncertainty), taking into consideration the relatively unfavourable geometry of the DAS array.

In view of the advantages and drawbacks of DAS and conventional seismometers, we recommend that the passive nature of DAS be leveraged to anticipate for future aftershock sequences in specific regions: rapid-access agreements with telecom operators can be struck at any given time, and dedicated fibre deployments can be made in areas where telecommunications infrastructures are sparse or lacking; preliminary noise floor assessments can be conducted and various optimisations can be considered; by combining DAS with a (permanent) seismic network, DAS strain recordings can be converted into particle motions (improving the signal characteristics) and small-magnitude events that fall within the DAS noise floor can be relocated with a limited number of seismometers relative to a well-recorded event absolutely located by DAS. In this way, the rapidity and "large N" characteristics of DAS are optimally combined with the high sensitivity of conventional seismometers.

Acknowledgements

MvdE is supported by the European Research Council (ERC) under the European Union's Horizon 2020 research and innovation programme (grant agreement No. 101041092 – ABYSS). JPA was supported by the French government

through the UCA^{JEDI} Investments in the Future project (ANR-15-IDEX-01) managed by the National Research Agency (ANR). The DAS measurements were made possible thanks to Febus Optics, the Ardèche Drôme Numérique telecom network, and the help of the ADTIM company. The following Python libraries were used for processing and visualisation of the data: JAX (Bradbury et al., 2020), NumPy (Harris et al., 2020), SciPy (Virtanen et al., 2019), Pandas (Pandas Development Team, 2020), ObsPy (Beyreuther et al., 2010), Cartopy (Met Office, 2015), Matplotlib (Hunter, 2007), Scientific Colourmaps (Crameri et al., 2020). Regional topography data were extracted from the European Digital Elevation Model (EU-DEM; version 1.1).

Data and code availability

All the data and scripts necessary to reproduce the results of this study are available from the following Zenodo repository: https://doi.org/10.5281/zenodo.10581351.

Competing interests

The authors declare no competing interests.

References

Ajo-Franklin, J. B., Dou, S., Lindsey, N. J., Monga, I., Tracy, C., Robertson, M., Rodriguez Tribaldos, V., Ulrich, C., Freifeld, B., Daley, T., and Li, X. Distributed Acoustic Sensing Using Dark Fiber for Near-Surface Characterization and Broadband Seismic Event Detection. *Scientific Reports*, 9(1):1–14, Feb. 2019. doi: 10.1038/s41598-018-36675-8.

Becker, J. S., Potter, S. H., McBride, S. K., H. Doyle, E. E., Gerstenberger, M. C., and Christophersen, A. Forecasting for a Fractured Land: A Case Study of the Communication and Use of Aftershock Forecasts from the 2016 Mw 7.8 Kaikōura Earthquake in Aotearoa New Zealand. *Seismological Research Letters*, 91(6):3343–3357, Sept. 2020. doi: 10.1785/0220190354.

Bertrand, E., Cornou, C., Gélis, C., Rivet, D., and SISMOB-RESIF. Le Teil P5 Post Seismic Experiment. 2019. doi: 10.15778/RESIF.3C2019.

Beyreuther, M., Barsch, R., Krischer, L., Megies, T., Behr, Y., and Wassermann, J. ObsPy: A Python Toolbox for Seismology. *Seismological Research Letters*, 81(3):530–533, May 2010. doi: 10.1785/gssrl.81.3.530.

Bonijoly, D., Perrin, J., Roure, F., Bergerat, F., Courel, L., Elmi, S., and Mignot, A. The Ardèche Palaeomargin of the South-East Basin of France: Mesozoic Evolution of a Part of the Tethyan Continental Margin (Géologie Profonde de La France Programme). *Marine and Petroleum Geology*, 13(6):607–623, Sept. 1996. doi: 10.1016/0264-8172(95)00075-5.

Bradbury, J., Frostig, R., Hawkins, P., Johnson, M. J., Leary, C., Maclaurin, D., Necula, G., Paszke, A., VanderPlas, J., Wanderman-Milne, S., and Zhang, Q. JAX: Composable Transformations of Python+NumPy Programs, 2020.

Calais, E., Symithe, S., Monfret, T., Delouis, B., Lomax, A., Courboulex, F., Ampuero, J. P., Lara, P. E., Bletery, Q., Chèze, J., Peix, F., Deschamps, A., de Lépinay, B., Raimbault, B., Jolivet, R., Paul, S., St Fleur, S., Boisson, D., Fukushima, Y., Duputel, Z., Xu, L., and Meng, L. Citizen Seismology Helps Decipher the 2021 Haiti Earthquake. *Science*, 376(6590):283–287, Apr. 2022. doi: 10.1126/science.abn1045.

Causse, M., Cornou, C., Maufroy, E., Grasso, J.-R., Baillet, L., and El Haber, E. Exceptional Ground Motion during the Shallow Mw 4.9 2019 Le Teil Earthquake, France. *Communications Earth & Environment*, 2(1):14, Jan. 2021. doi: 10.1038/s43247-020-00089-0.

Cerveny, V. *Seismic Ray Theory*. Cambridge University Press, 1 edition, July 2001. doi: 10.1017/CBO9780511529399.

Cornou, C., Ampuero, J.-P., Aubert, C., Audin, L., Baize, S., Billant, J., Brenguier, F., Causse, M., Chlieh, M., Combey, A., de Michele, M., Delouis, B., Deschamps, A., Ferry, M., Foumelis, M., Froment, B., Gélis, C., Grandin, R., Grasso, J.-R., Hannouz, E., Hok, S., Jung, A., Jolivet, R.,

Langlais, M., Langlaude, P., Larroque, C., Leloup, P. H., Manchuel, K., Marconato, L., Maron, C., Mathot, E., Maufroy, E., Mercerat, D., Metois, M., Nayman, E., Pondaven, I., Provost, L., Régnier, J., Ritz, J.-F., Rivet, D., Schlupp, A., Sladen, A., Voisin, C., Walpersdorf, A., Wolynieck, D., Allemand, P., Beck, E., Bertrand, E., Bertrand, V., Briole, P., Brunel, D., Cavalié, O., Chèze, J., Courboulex, F., Douste-Bacque, I., Dretzen, R., Giampietro, T., Godano, M., Grandjean, P., Grunberg, M., Guerin, G., Guillot, S., Haber, E. E., Hernandez, A., Jomard, H., Lasserre, C., Liang, C., Lior, I., Martin, X., Mata, D., Menager, M., Mercier, A., Mordret, A., Oral, E., Paul, A., Peix, F., Pequegnat, C., Pernoud, M., Satriano, C., Sassi, R., Schaming, M., Sellier, V., Sira, C., Socquet, A., Sue, C., Trilla, A., Vallée, M., van den Ende, M., Vernant, P., Vial, B., and Weng, H. Rapid Response to the M w 4.9 Earthquake of November 11, 2019 in Le Teil, Lower Rhône Valley, France. *Comptes Rendus. Géoscience*, 353(S1):1–23, Mar. 2021. doi: 10.5802/crgeos.30.

Correa, J., Egorov, A., Tertyshnikov, K., Bona, A., Pevzner, R., Dean, T., Freifeld, B., and Marshall, S. Analysis of Signal to Noise and Directivity Characteristics of DAS VSP at near and Far Offsets — A CO2CRC Otway Project Data Example. *The Leading Edge*, 36(12):994a1–994a7, Dec. 2017. doi: 10.1190/tle36120994a1.1.

Crameri, F., Shephard, G. E., and Heron, P. J. The Misuse of Colour in Science Communication. *Nature Communications*, 11(1):5444, Oct. 2020. doi: 10.1038/s41467-020-19160-7.

Daley, T. M., Miller, D. E., Dodds, K., Cook, P., and Freifeld, B. M. Field Testing of Modular Borehole Monitoring with Simultaneous Distributed Acoustic Sensing and Geophone Vertical Seismic Profiles at Citronelle, Alabama. *Geophysical Prospecting*, 64(5):1318–1334, 2016. doi: 10.1111/1365-2478.12324.

Danciu, L., Nandan, S., Reyes, C., Basili, R., Weatherill, G., Beauval, C., Rovida, A., Vilanova, S., Sesetyan, K., Bard, P.-Y., Cotton, F., Wiemer, S., and Giardini, D. ESHM20 - EFEHR Technical ReportThe 2020 Update of the European Seismic Hazard Model - ESHM20: Model Overview. Technical report, EFEHR European Facilities of Earthquake Hazard and Risk, 2021.

Delouis, B., Oral, E., Menager, M., Ampuero, J.-P., Guilhem Trilla, A., Régnier, M., and Deschamps, A. Constraining the Point Source Parameters of the 11 November 2019 Mw 4.9 Le Teil Earthquake Using Multiple Relocation Approaches, First Motion and Full Waveform Inversions. *Comptes Rendus. Géoscience*, 353(S1):493–516, Jan. 2022. doi: 10.5802/crgeos.78.

Delouis, B., van den Ende, M., and Ampuero, J.-P. Kinematic Rupture Model of the February 6th 2023 Mw7.8 Turkey Earthquake from a Large Set of near-Source Strong Motion Records Combined by GNSS Offsets Reveals Intermittent Supershear Rupture. Preprint, Preprints, Apr. 2023.

Dou, S., Lindsey, N., Wagner, A. M., Daley, T. M., Freifeld, B., Robertson, M., Peterson, J., Ulrich, C., Martin, E. R., and Ajo-Franklin, J. B. Distributed Acoustic Sensing for Seismic Monitoring of The Near Surface: A Traffic-Noise Interferometry Case Study. *Scientific Reports*, 7 (1):11620, Sept. 2017. doi: 10.1038/s41598-017-11986-4.

Font, Y., Kao, H., Lallemand, S., Liu, C.-S., and Chiao, L.-Y. Hypocentre Determination Offshore of Eastern Taiwan Using the Maximum Intersection Method. *Geophysical Journal International*, 158(2):655–675, Aug. 2004. doi: 10.1111/j.1365-246X.2004.02317.x.

Gibbons, S. J. and Ringdal, F. The Detection of Low Magnitude Seismic Events Using Array-Based Waveform Correlation. *Geophysical Journal International*, 165(1):149–166, Apr. 2006. doi: 10.1111/j.1365-246X.2006.02865.x.

Harris, C. R., Millman, K. J., van der Walt, S. J., Gommers, R., Virtanen, P., Cournapeau, D., Wieser, E., Taylor, J., Berg, S., Smith, N. J., Kern, R., Picus, M., Hoyer, S., van Kerkwijk, M. H., Brett, M., Haldane, A., del Río, J. F., Wiebe, M., Peterson, P., Gérard-Marchant, P., Sheppard, K., Reddy, T., Weckesser, W., Abbasi, H., Gohlke, C., and Oliphant, T. E. Array Programming with NumPy. *Nature*, 585(7825):357–362, Sept. 2020. doi: 10.1038/s41586-020-2649-2.

Hartog, A. H. *An Introduction to Distributed Optical Fibre Sensors*. CRC Press, May 2017. doi: 10.1201/9781315119014.

Hauksson, E., Yoon, C., Yu, E., Andrews, J. R., Alvarez, M., Bhadha, R., and Thomas, V. Caltech/USGS Southern California Seismic Network (SCSN) and Southern California Earthquake Data Center (SCEDC): Data Availability for the 2019 Ridgecrest Sequence. *Seismological*

Research Letters, 91(4):1961–1970, Jan. 2020. doi: 10.1785/0220190290.

Hunter, J. D. Matplotlib: A 2D Graphics Environment. *Computing in Science & Engineering*, 9(3):90–95, 2007. doi: 10.1109/MCSE.2007.55.

Hutchison, A. A. and Ghosh, A. Repeating VLFEs During ETS Events in Cascadia Track Slow Slip and Continue Throughout Inter-ETS Period. *Journal of Geophysical Research: Solid Earth*, 124(1):554–565, 2019. doi: 10.1029/2018JB016138.

Ide, S., Araki, E., and Matsumoto, H. Very Broadband Strain-Rate Measurements along a Submarine Fiber-Optic Cable off Cape Muroto, Nankai Subduction Zone, Japan. *Earth, Planets and Space*, 73(1):63, Mar. 2021. doi: 10.1186/s40623-021-01385-5.

Ip, E., Huang, Y.-K., Huang, M.-F., Yaman, F., Wellbrock, G., Xia, T., Wang, T., Asahi, K., and Aono, Y. DAS Over 1,007-Km Hybrid Link With 10-Tb/s DP-16QAM Co-propagation Using Frequency-Diverse Chirped Pulses. *Journal of Lightwave Technology*, pages 1–10, 2022. doi: 10.1109/JLT.2022.3219369.

Jousset, P., Reinsch, T., Ryberg, T., Blanck, H., Clarke, A., Aghayev, R., Hersir, G. P., Henninges, J., Weber, M., and Krawczyk, C. M. Dynamic Strain Determination Using Fibre-Optic Cables Allows Imaging of Seismological and Structural Features. *Nature Communications*, 9(1): 2509, July 2018. doi: 10.1038/s41467-018-04860-y.

Jousset, P., Currenti, G., Schwarz, B., Chalari, A., Tilmann, F., Reinsch, T., Zuccarello, L., Privitera, E., and Krawczyk, C. M. Fibre Optic Distributed Acoustic Sensing of Volcanic Events. *Nature Communications*, 13(1):1753, Mar. 2022. doi: 10.1038/s41467-022-29184-w.

Kingma, D. P. and Ba, J. Adam: A Method for Stochastic Optimization. *arXiv:1412.6980 [cs]*, Jan. 2017.

Kuvshinov, B. N. Interaction of Helically Wound Fibre-Optic Cables with Plane Seismic Waves. *Geophysical Prospecting*, 64(3):671–688, 2016. doi: 10.1111/1365-2478.12303.

Larroque, C., Baize, S., Albaric, J., Jomard, H., Trévisan, J., Godano, M., Cushing, M., Deschamps, A., Sue, C., Delouis, B., Potin, B., Courboulex, F., Régnier, M., Rivet, D., Brunel, D., Chèze, J., Martin, X., Maron, C., and Peix, F. Seismotectonics of Southeast France: From the Jura Mountains to Corsica. *Comptes Rendus. Géoscience*, 353(S1):105–151, Jan. 2022. doi: 10.5802/crgeos.69.

Lengliné, O., Duputel, Z., and Ferrazzini, V. Uncovering the Hidden Signature of a Magmatic Recharge at Piton de La Fournaise Volcano Using Small Earthquakes. *Geophysical Research Letters*, 43(9):4255–4262, 2016. doi: 10.1002/2016GL068383.

Li, Z. and Zhan, Z. Pushing the Limit of Earthquake Detection with Distributed Acoustic Sensing and Template Matching: A Case Study at the Brady Geothermal Field. *Geophysical Journal International*, 215(3):1583–1593, Dec. 2018. doi: 10.1093/gji/ggy359.

Li, Z., Shen, Z., Yang, Y., Williams, E., Wang, X., and Zhan, Z. Rapid Response to the 2019 Ridgecrest Earthquake With Distributed Acoustic Sensing. *AGU Advances*, 2(2):e2021AV000395, 2021. doi: 10.1029/2021AV000395.

Lior, I., Sladen, A., Rivet, D., Ampuero, J.-P., Hello, Y., Becerril, C., Martins, H. F., Lamare, P., Jestin, C., Tsagkli, S., and Markou, C. On the Detection Capabilities of Underwater DAS. *Journal of Geophysical Research: Solid Earth*, n/a(n/a):e2020JB020925, 2021. doi: 10.1029/2020JB020925.

Liu, Q. and Wang, D. Stein Variational Gradient Descent: A General Purpose Bayesian Inference Algorithm. In *Advances in Neural Information Processing Systems*, volume 29. Curran Associates, Inc., 2016.

Lomax, A., Virieux, J., Volant, P., and Berge-Thierry, C. Probabilistic Earthquake Location in 3D and Layered Models. In Nolet, G., Thurber, C. H., and Rabinowitz, N., editors, *Advances in Seismic Event Location*, volume 18, pages 101–134. Springer Netherlands, Dordrecht, 2000. doi: 10.1007/978-94-015-9536-0$_5$.

Luo, B., Jin, G., and Stanek, F. Near-Field Strain in Distributed Acoustic Sensing-Based Microseismic observationDAS Microseismic near-Field Strain. *Geophysics*, pages P49–P60, 2021. doi: 10.1190/geo2021-0031.1.

Marconato, L., Leloup, P. H., Lasserre, C., Jolivet, R., Caritg, S., Grandin, R., Métois, M., Cavalié, O., and Audin, L. Insights on Fault Reactivation during the 2019 November 11, *M* w 4.9 Le Teil Earthquake in Southeastern France, from a Joint 3-D Geological Model and InSAR Time-

Series Analysis. *Geophysical Journal International*, 229(2):758–775, Jan. 2022. doi: 10.1093/gji/ggab498.

Melgar, D., Taymaz, T., Ganas, A., Crowell, B., Öcalan, T., Kahraman, M., Tsironi, V., Yolsal-Çevikbil, S., Valkaniotis, S., Irmak, T. S., Eken, T., Erman, C., Özkan, B., Dogan, A. H., and Altuntaş, C. Sub- and Super-Shear Ruptures during the 2023 Mw 7.8 and Mw 7.6 Earthquake Doublet in SE Türkiye. *Seismica*, 2(3), Mar. 2023. doi: 10.26443/seismica.v2i3.387.

Met Office, t. Cartopy: A Cartographic Python Library with a Matplotlib Interface, 2015.

Michael, A. J., McBride, S. K., Hardebeck, J. L., Barall, M., Martinez, E., Page, M. T., van der Elst, N., Field, E. H., Milner, K. R., and Wein, A. M. Statistical Seismology and Communication of the USGS Operational Aftershock Forecasts for the 30 November 2018 Mw 7.1 Anchorage, Alaska, Earthquake. *Seismological Research Letters*, 91(1):153–173, Jan. 2020. doi: 10.1785/0220190196.

Pandas Development Team, t. Pandas-Dev/Pandas: Pandas. Zenodo, 2020.

Rawlinson, N., Hauser, J., and Sambridge, M. Seismic Ray Tracing and Wavefront Tracking in Laterally Heterogeneous Media. In Dmowska, R., editor, *Advances in Geophysics*, volume 49, pages 203–273. Elsevier, Jan. 2008. doi: 10.1016/S0065-2687(07)49003-3.

Reasenberg, P. A. and Jones, L. M. Earthquake Hazard After a Mainshock in California. *Science*, 243(4895):1173–1176, Mar. 1989. doi: 10.1126/science.243.4895.1173.

Ritz, J.-F., Baize, S., Ferry, M., Larroque, C., Audin, L., Delouis, B., and Mathot, E. Surface Rupture and Shallow Fault Reactivation during the 2019 Mw 4.9 Le Teil Earthquake, France. *Communications Earth & Environment*, 1(1):10, Aug. 2020. doi: 10.1038/s43247-020-0012-z.

Ross, Z. E., Yue, Y., Meier, M.-A., Hauksson, E., and Heaton, T. H. PhaseLink: A Deep Learning Approach to Seismic Phase Association. *Journal of Geophysical Research: Solid Earth*, 124(1):856–869, 2019. doi: 10.1029/2018JB016674.

Roure, F., Brun, J.-P., Colletta, B., and Van Den Driessche, J. Geometry and Kinematics of Extensional Structures in the Alpine Foreland Basin of Southeastern France. *Journal of Structural Geology*, 14(5):503–519, May 1992. doi: 10.1016/0191-8141(92)90153-N.

Savage, H. M., Kirkpatrick, J. D., Mori, J. J., Brodsky, E. E., Ellsworth, W. L., Carpenter, B. M., Chen, X., Cappa, F., and Kano, Y. Scientific Exploration of Induced SeisMicity and Stress (SEISMS). *Scientific Drilling*, 23:57–63, Nov. 2017. doi: 10.5194/sd-23-57-2017.

Schneider, M., McDowell, M., Guttorp, P., Steel, E. A., and Fleischhut, N. Effective Uncertainty Visualization for Aftershock Forecast Maps. *Natural Hazards and Earth System Sciences*, 22(4):1499–1518, Apr. 2022. doi: 10.5194/nhess-22-1499-2022.

Shelly, D. R. A High-Resolution Seismic Catalog for the Initial 2019 Ridgecrest Earthquake Sequence: Foreshocks, Aftershocks, and Faulting Complexity. *Seismological Research Letters*, 91(4):1971–1978, Jan. 2020. doi: 10.1785/0220190309.

Shelly, D. R., Beroza, G. C., and Ide, S. Non-Volcanic Tremor and Low-Frequency Earthquake Swarms. *Nature*, 446(7133):305–307, Mar. 2007. doi: 10.1038/nature05666.

Sladen, A., Rivet, D., Ampuero, J. P., De Barros, L., Hello, Y., Calbris, G., and Lamare, P. Distributed Sensing of Earthquakes and Ocean-Solid Earth Interactions on Seafloor Telecom Cables. *Nature Communications*, 10(1):1–8, Dec. 2019. doi: 10.1038/s41467-019-13793-z.

Smith, J. D., Ross, Z. E., Azizzadenesheli, K., and Muir, J. B. HypoSVI: Hypocentre Inversion with Stein Variational Inference and Physics Informed Neural Networks. *Geophysical Journal International*, 228(1):698–710, Jan. 2022. doi: 10.1093/gji/ggab309.

Thouvenot, F., Fréchet, J., Tapponnier, P., Thomas, J.-C., Le Brun, B., Ménard, G., Lacassin, R., Jenatton, L., Grasso, J.-R., Coutant, O., Paul, A., and Hatzfeld, D. The ML 5.3 Epagny (French Alps) Earthquake of 1996 July 15: A Long-Awaited Event on the Vuache Fault. *Geophysical Journal International*, 135(3):876–892, Dec. 1998. doi: 10.1046/j.1365-246X.1998.00662.x.

Trabattoni, A., Biagioli, F., Strumia, C., van den Ende, M., Scotto di Uccio, F., Festa, G., Rivet, D., Sladen, A., Ampuero, J. P., Métaxian, J.-P., and Stutzmann, É. From Strain to Displacement: Using Deformation to Enhance Distributed Acoustic Sensing Applications. *Geophysical Journal International*, 235(3):2372–2384, Dec. 2023. doi: 10.1093/gji/ggad365.

Vallage, A., Bollinger, L., Champenois, J., Duverger, C., Trilla, A. G., Hernandez, B., Pichon, A. L., Listowski, C., Mazet-Roux, G., Menager, M.,

583 Pinel-Puysségur, B., and Vergoz, J. Multitechnology Characterization of an Unusual Surface Rupturing Intraplate Earthquake: The *M* L
584 5.4 2019 Le Teil Event in France. *Geophysical Journal International*, 226(2):803–813, May 2021. doi: 10.1093/gji/ggab136.

585 van den Ende, M., Ferrari, A., Sladen, A., and Richard, C. Deep Deconvolution for Traffic Analysis With Distributed Acoustic Sensing Data.
586 *IEEE Transactions on Intelligent Transportation Systems*, pages 1–0, 2022. doi: 10.1109/TITS.2022.3223084.

587 van den Ende, M. P. A. and Ampuero, J.-P. Evaluating Seismic Beamforming Capabilities of Distributed Acoustic Sensing Arrays. *Solid Earth*,
588 12(4):915–934, Apr. 2021. doi: 10.5194/se-12-915-2021.

589 Virtanen, P., Gommers, R., Oliphant, T. E., Haberland, M., Reddy, T., Cournapeau, D., Burovski, E., Peterson, P., Weckesser, W., Bright, J., van
590 der Walt, S. J., Brett, M., Wilson, J., Millman, K. J., Mayorov, N., Nelson, A. R. J., Jones, E., Kern, R., Larson, E., Carey, C. J., Polat, İ., Feng,
591 Y., Moore, E. W., VanderPlas, J., Laxalde, D., Perktold, J., Cimrman, R., Henriksen, I., Quintero, E. A., Harris, C. R., Archibald, A. M., Ribeiro,
592 A. H., Pedregosa, F., van Mulbregt, P., and Contributors, S. . . SciPy 1.0–Fundamental Algorithms for Scientific Computing in Python.
593 *arXiv:1907.10121 [physics]*, July 2019.

594 Waldhauser, F. and Ellsworth, W. L. A Double-Difference Earthquake Location Algorithm: Method and Application to the Northern Hayward
595 Fault, California. *Bulletin of the Seismological Society of America*, 90(6):1353–1368, Dec. 2000. doi: 10.1785/0120000006.

596 Wang, H. F., Zeng, X., Miller, D. E., Fratta, D., Feigl, K. L., Thurber, C. H., and Mellors, R. J. Ground Motion Response to an ML 4.3 Earthquake
597 Using Co-Located Distributed Acoustic Sensing and Seismometer Arrays. *Geophysical Journal International*, 213(3):2020–2036, June
598 2018. doi: 10.1093/gji/ggy102.

599 Welch, P. The Use of Fast Fourier Transform for the Estimation of Power Spectra: A Method Based on Time Averaging over Short, Modified
600 Periodograms. *IEEE Transactions on Audio and Electroacoustics*, 15(2):70–73, June 1967. doi: 10.1109/TAU.1967.1161901.

601 Wu, M., Li, C., Fan, X., Liao, C., and He, Z. Large-Scale Multiplexed Weak Reflector Array Fabricated with a Femtosecond Laser for a Fiber-Optic
602 Quasi-Distributed Acoustic Sensing System. *Optics Letters*, 45(13):3685–3688, July 2020. doi: 10.1364/OL.395725.

SEISMICA

Distributed Acoustic Sensing for aftershock monitoring: the case of the 2019 M_w 4.9 Le Teil earthquake

Martijn van den Ende * [1], **Jean-Paul Ampuero** [1], **Françoise Courboulex** [1], **Bertrand Delouis** [1], **Maxime Godano** [1], **Christophe Larroque** [1,2], **Anthony Sladen** [1]

[1]Université Côte d'Azur, CNRS, IRD, Observatoire de la Côte d'Azur, Géoazur, France, [2]Université de Reims Champagne-Ardenne, GEGENAA, Reims, France

Contents:

*Corresponding author: martijn.vandenende@oca.eu

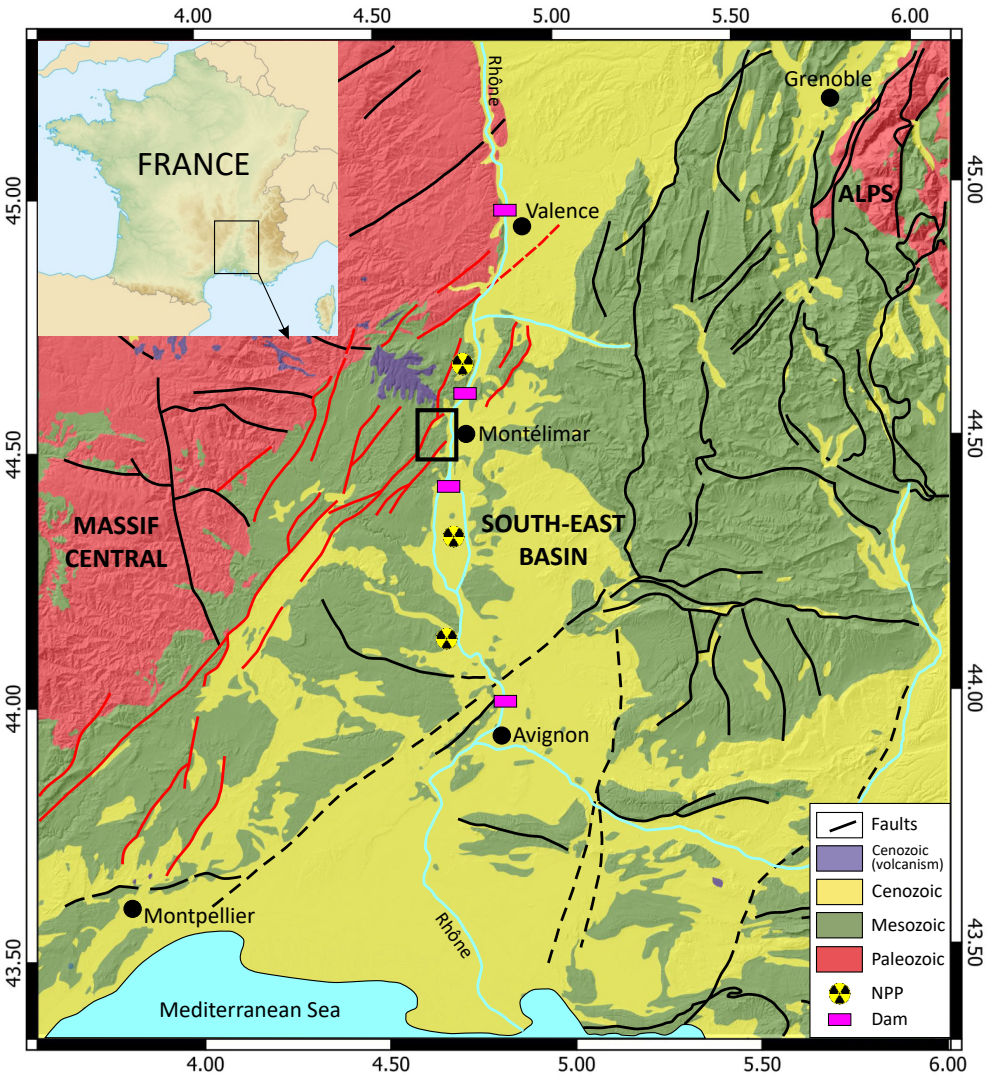

Figure S1 Tectonic setting of the Le Teil epicentral region. The area of study is positioned within the black box near the centre of the figure (west of Montélimar). Also indicated are nuclear powerplants (NPP) and major dams along the Rhône river.

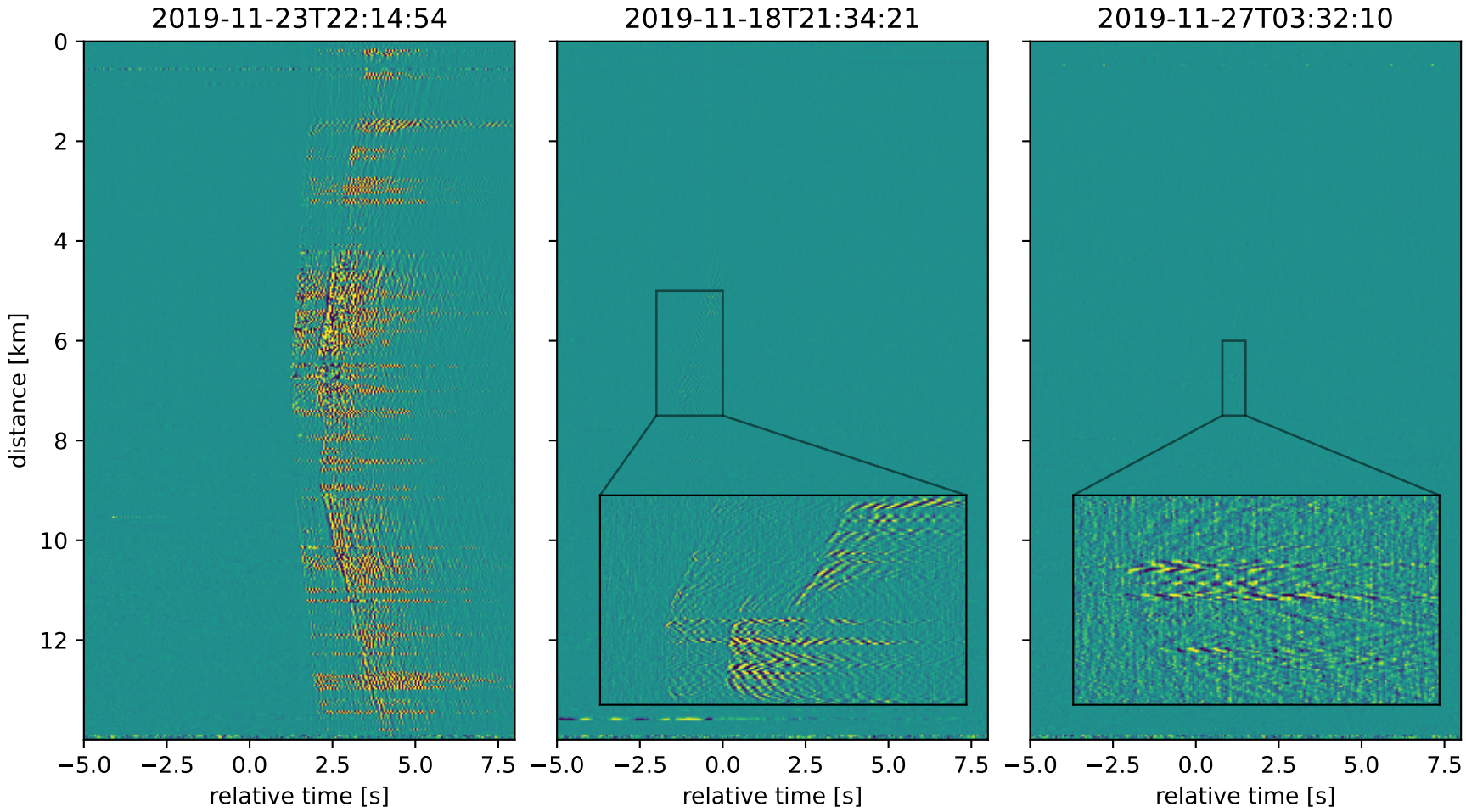

Figure S2 DAS recordings of three selected aftershocks with largest estimated magnitudes, in descending order of signal-to-noise ratio. While the principal aftershock has a reasonable SNR over most of the cable, the signal amplitudes of the other two events barely exceed the noise level. Each of the three main panels has the same colour range, but the colour range of the insets is adjusted to highlight the details of each event. The origin time of each event is as indicated above each panel.

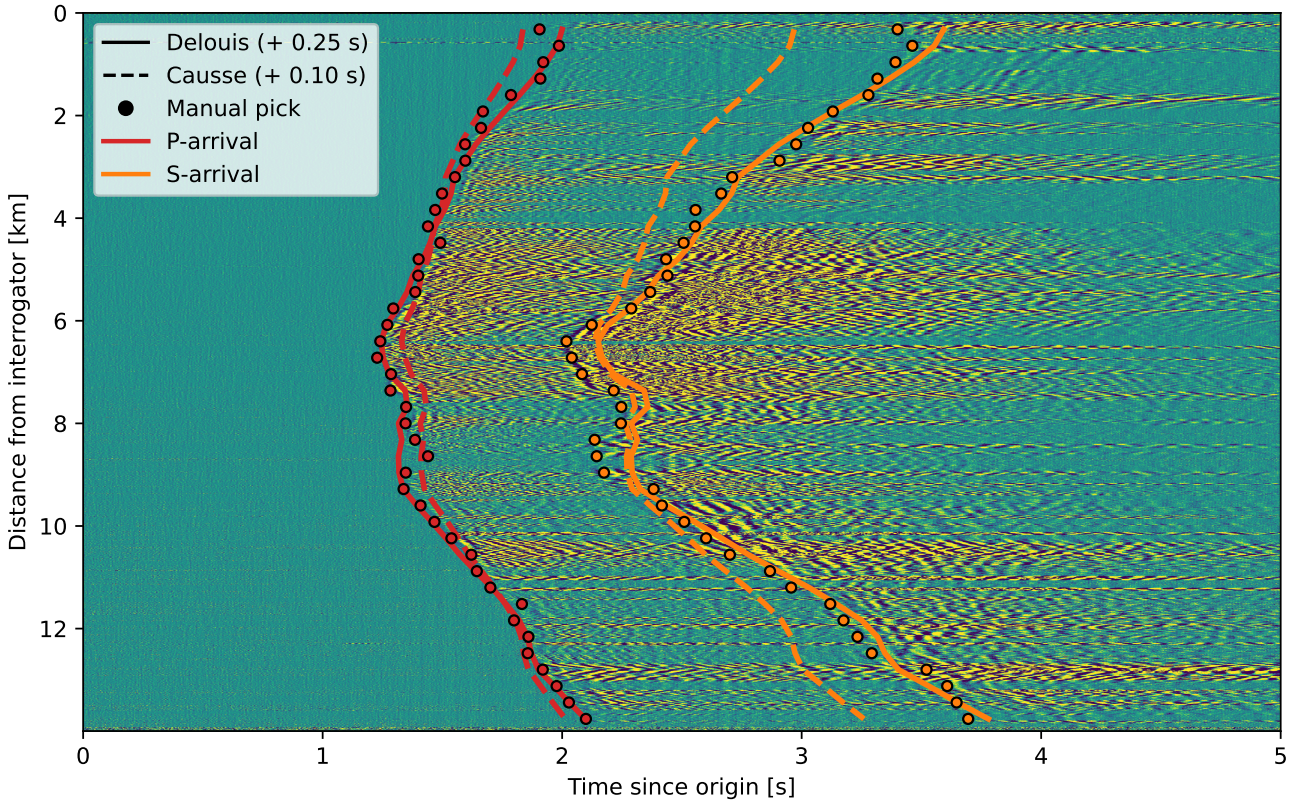

Figure S3 Comparison of two proposed velocity models with DAS recordings. Manual picks of the first P- and S-phase arrivals were made every 100 channels (solid disks). The corresponding arrival times predicted for the constant-gradient model proposed by Delouis et al. (2022), and the layered model proposed by Causse et al. (2021) are indicated by the solid and dashed lines, respectively. For each velocity model, the corresponding hypocentre location and origin time were used (i.e., which were inverted assuming each given velocity model). The optimal fit with the observed P-arrivals is obtained by shifting the origin time by $+0.25$ s for the model of Delouis et al. (2022), and by $+0.10$ s for that of Causse et al. (2021). The largest discrepancy between the two velocity models is seen for the S-arrivals; it is apparent that the velocity model of Causse et al. (2021) exhibits an average S-wave speed that is too low. The velocity model of Delouis et al. (2022) overall has a satisfactory fit, motivating our choice for this velocity model for the SVI inversion.

Station code	Latitude [°]	Longitude [°]	Elevation [m]	P-pick	S-pick
ALBA	44.554879	4.603087	220	1.02	2.39
AUBI	44.5769	4.62346	326	1.16	2.68
BEAU	44.500019	4.627541	150	0.594	1.489
CAMP	44.4892	4.6766	116	0.41	1.06
CROT	44.50289	4.626209	115	0.594	1.453
ILES	44.52557	4.71973	75	0.5	1.409
LAFA	44.5137	4.6636	273	0.084	0.468
LARN	44.44704	4.59211	310	1.877	3.864
MONN	44.5838	4.7499	70	1.567	3.32
N01	44.497517	4.653054	105	0.373	0.961
N02	44.522556	4.620619	157	0.593	1.571
N03	44.519306	4.646326	328	0.233	0.8
N04	44.522254	4.654546	266	0.151	0.593
N05	44.54181	4.65486	155	0.332	0.952
N06	44.549888	4.631562	217	0.699	1.64
N07	44.52917	4.664568	185	0.064	0.368
N08	44.512191	4.685316	68	0.08	0.42
N09	44.513403	4.653802	186	0.171	0.622
N10	44.515146	4.663737	91	0.06	0.452
N11	44.511593	4.634662	270	0.409	-
N12	44.512454	4.635169	273	0.405	1.102
N13	44.512364	4.634686	265	0.405	1.101
N14	44.511675	4.635292	270	0.405	1.1
N15	44.512089	4.634934	272	0.405	1.1
N16	44.487922	4.61879	122	0.85	1.927
N17	44.482045	4.690227	71	0.542	1.363
N18	44.558621	4.61742	300	0.942	2.27
N19	44.481999	4.690224	71	0.54	1.374
N20	44.482053	4.690195	71	0.537	1.463
N21	44.548453	4.632406	205	0.668	1.657
N22	44.548459	4.630398	199	0.687	1.666
N23	44.55187	4.632665	225	0.714	1.69
N24	44.550611	4.631682	215	0.71	1.713
N25	44.512164	4.685332	68	0.081	0.55
N26	44.513731	4.643173	279	0.285	0.898
N27	44.511956	4.685299	68	0.086	0.563
N28	44.482041	4.690065	71	0.54	1.344
STIL	44.52256	4.62061	155	0.593	1.55
TEIL	44.550396	4.683843	70	0.449	1.166
THOC	44.502632	4.622869	147	0.65	1.549
THOM	44.500429	4.626154	231	0.613	1.508
VIVI	44.479933	4.691403	119	0.561	1.518

Table S4 Seismic stations used in the study, their location, and manually picked phase arrivals. The arrival times are relative to 2019-11-23 22:14:55 UTC. This table is available in CSV format as a separate supplement, and from the code repository (see acknowledgements in the main text).

References

Causse, M., Cornou, C., Maufroy, E., Grasso, J.-R., Baillet, L., and El Haber, E. Exceptional Ground Motion during the Shallow Mw 4.9 2019 Le Teil Earthquake, France. *Communications Earth & Environment*, 2(1):14, Jan. 2021. doi: 10.1038/s43247-020-00089-0.

Delouis, B., Oral, E., Menager, M., Ampuero, J.-P., Guilhem Trilla, A., Régnier, M., and Deschamps, A. Constraining the Point Source Parameters of the 11 November 2019 Mw 4.9 Le Teil Earthquake Using Multiple Relocation Approaches, First Motion and Full Waveform Inversions. *Comptes Rendus. Géoscience*, 353(S1): 493–516, Jan. 2022. doi: 10.5802/crgeos.78.